On the Oblique Impact Dynamics of Drops on Superhydrophobic Surfaces. Part I: Sliding Length and Maximum Spreading Diameter

*Damon G. K. Aboud, Anne-Marie Kietzig**

Department of Chemical Engineering, McGill University, Montreal QC, H3A 0C5 Canada

KEYWORDS

Drops, wetting, drop impact, oblique drop impact, Weber numbers, superhydrophobicity, oblique impact, inclined surface, angle of incidence, drop spreading.

ABSTRACT

Oblique water drop impacts were performed on a superhydrophobic surface at normal Weber numbers in the range of $3 < We_n < 80$ and at angles of incidence ranging from 0 < AOI < 60°. While holding We_n constant, we varied the AOI to investigate how the oblique nature of the impact affects the sliding length and spreading diameter of impacting drops. Our sliding length measurements indicate that drops impacting at We_n < 10 retain essentially full mobility on the surface, whereas the sliding of higher-We_n impacts is inhibited by drag forces. We attribute this trend to increased penetration into air-trapping surface features occurring in higher-We_n impacts,

which results in more adhesion between the liquid and solid. Regarding the spreading of drops on SHP surfaces, the dimensionless maximum spread diameter (D^*_{max}) increases not only with We_n, but also with the angle of incidence, such that more oblique drop impacts stretch to a wider maximum diameter. We attribute this behaviour to adhesion forces, which act to stretch the drop as it slides tangentially across the surface in oblique impacts. Based on this theory, we derived a model predicting D^*_{max} for any We_n and AOI. The model's predictions are highly accurate, successfully predicting D^*_{max} for our entire experimental space. Finally, by placing the camera above the sample, we observed that oblique drop impacts spread into an elliptical shape, and we present a model predicting the maximum spread area.

INTRODUCTION

Over the past two decades, superhydrophobic (SHP) surfaces have been a subject of great interest as a result of their incredible water repellent properties. Since SHP surfaces promote the complete rebounding of water drops, they have been considered for a number of different applications, such as anti-icing airplane wings and turbine blades [1], and water-shedding glass windows [2]. However, in order to design SHP surfaces for these applications, a fundamental understanding of single drop impact is first required. There is already a wealth of knowledge about drop impact behaviour at a normal angle of incidence [3-13]. However, real engineering applications require knowledge of how drops behave in oblique impacts, for which there remains relatively little information. Hence, this report focusses on the sliding length and maximum spread diameter of oblique impacting drops on SHP surfaces. Both of these parameters are especially important in the design of ice-proof surfaces, since an increased contact area between the drop and surface encourages more heat transfer, and more freezing [14].

A superhydrophobic surface is characterized by an advancing contact angle greater than 150°, as well as a low contact angle hysteresis (CAH) [15]. Usually, these wetting properties are observed on a surface that is chemically hydrophobic (such as PTFE), and whose topography is hierarchical, with a microstructure that is in turn covered by a nanostructure [16]. This allows for the Cassie wetting state, in which the droplet does not fully wet the solid surface, but instead makes contact only with the topographical peaks, leaving air pockets in the pores below. Accordingly, only a small fraction of the droplet's area makes physical contact with the solid, resulting in very low adhesion, and high mobility of the drop on the surface [16]. It is exactly this non-wetting behaviour that allows for the complete rebounding of water drops. During impact, the drop deforms against the surface, and ejects a thin liquid sheet called the lamella, which spreads radially outward from the impact center [7]. On a SHP surface, the low adhesion allows the lamella to retract back to the liquid bulk via surface tension, and the recombined droplet can leap off the surface.

Another important process that occurs during drop impact on a SHP surface is the partial penetration of the drop into the pores of the surface. This process occurs at the center of the impact site, and is caused by the dynamic pressure of impact (P_D). The dynamic pressure is caused by the drop's change in momentum as it strikes the surface, and scales as $P_D \sim \rho {v_{n1}}^2$, where ρ is the liquid density, and v_{n1} is the normal velocity of impact [17-19]. However, this force is opposed by the Laplace pressure (P_L), which is a manifestation of the surface tension, and is exerted by the curvature of the liquid within the pores. The magnitude of the Laplace pressure is given by $P_L = 2\sigma \cdot \cos(ACA)/R_L$, where σ is the surface tension of the liquid, ACA is the advancing contact angle, and R_L is the radius of curvature of the penetrating liquid [20]. During drop impact, the penetration depth of the liquid is governed by the competition between these two opposing forces.

Low-velocity impacts have a low P_D, and therefore a small penetration depth, whereas high-speed impacts exert a much greater P_D, resulting in deeper penetration.

To predict the impact behaviour, researchers have traditionally employed the normal Weber number, $We_n = \rho {v_{n1}}^2 D_0/\sigma$, with D_0 the initial drop diameter. The Weber number provides a comparison between the drop's inertial and surface tension forces, and thus expresses the competition between these two primary factors [8]. However, We_n alone can only describe the conditions of a normal drop impact. In order to describe oblique drop impacts, one must consider not only the normal velocity (v_{n1}), but also the tangential velocity (v_{t1}) and the angle of incidence (AOI). These parameters are illustrated in **Figure 1**, which provides a schematic of the angles and velocities involved. **Figure 1(a)** illustrates the geometry of our experiment, and depicts a drop with falling speed v_d, onto a surface moving horizontally with a speed of v_s, and with a tilt angle of θ. **Figure 1(b)** depicts the same system, but taking the sample surface as the point of reference, thereby taking into account its tilt angle and velocity. From this perspective, we find that the normal impact velocity is given by $v_{n1} = v_s\, sin(\theta) + v_d\, cos(\theta)$, and the tangential velocity by $v_{t1} = v_s\, cos(\theta) - v_d\, sin(\theta)$. The angle of incidence is then equal to:

$$AOI = tan^{-1}(v_{t1}/v_{n1}) \qquad \textbf{Equation 1}$$

such that normal impacts occur at AOI = 0°, and oblique impacts occur at higher AOI. Note that the AOI is different than the surface tilt angle, θ. While θ describes the tilt angle of the surface with respect to the horizontal plane, the AOI expresses the angle with which the droplet strikes the surface, with respect to the orientation and movement of the surface. The two are only of equal value if the surface is stationary.

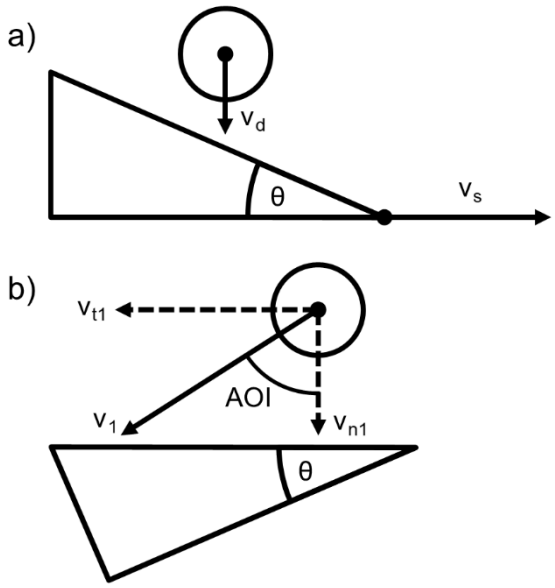

Figure 1. Schematic of our oblique drop impact experiment. (a) a drop falls downwards with a velocity of v_d, onto a surface moving at a velocity of v_s, with a surface tilt of θ. (b) The same drop and surface as above, but taking the surface as the frame of reference. The drop's impact velocity with respect to the surface (v_1) can be separated into a tangential (v_{t1}) and a normal (v_{n1}) component. The angle of incidence of the impact depends on v_{n1} and v_{t1}.

In the past, many researchers have used We_n to predict the drop's dimensionless maximum spread diameter, ($D^*_{max} = D_{max}/D_0$). For drops impacting at We_n below about 10, surface tension competes with the inertia of the impact, and the droplet retains a relatively spherical shape, spreading over a marginal area of the surface. At higher We_n, the deformation becomes more significant as the drop spreads into a pancake shape, extending to a greater maximum diameter. To this day, there remains some debate about the exact relationship between D^*_{max} and We_n, which is critical towards understanding the transfer of the impacting drop's kinetic energy into surface energy. Applying an energy balance for the case of lossless energy transfer, one finds that the

maximum spread diameter should scale according to the relationship $D^*_{max} \sim We_n^{1/2}$ [9]. However, this ignores losses due to viscous dissipation. Alternatively, by considering the drop's capillary length, in conjunction with the acceleration imparted on the drop by the solid surface, Clanet et al. (2004) have presented a convincing derivation indicating that $D^*_{max} \sim We_n^{1/4}$ [9]. In practice, the true relationship tends to lie somewhere within these two boundaries, and varies among different studies depending on the surface tested. For normal drop impacts, some reported values include $D^*_{max} \sim We_n^{1/4}$ [4, 5, 9, 13, 21], $D^*_{max} \sim We_n^{0.31}$ [22], $D^*_{max} \sim We_n^{0.34}$ [6], and $D^*_{max} \sim We_n^{1/2}$ [23]. Furthermore, in the case of oblique impacts, the drop's tangential velocity results in a greater spread diameter. Yeong et al. (2014) observed droplets in oblique impacts on a SHP surface, and found that for impacts occurring at constant We_n, the spreading diameter increases at higher AOI [21].

Beyond the drop's spread diameter, oblique impacting droplets also slide tangentially across the face of the solid surface during their interaction. For an impact with a tangential velocity of v_{t1} onto a surface tilted at θ, and neglecting energy losses due to drag, one would expect the droplet to travel an idealized sliding length (L_0) of:

$$L_0 = v_{t1} t_c + \frac{1}{2} g \cdot \sin(\theta) \cdot {t_c}^2 \qquad \textbf{Equation 2}$$

where t_c is the drop's contact time on the surface, and g is acceleration due to gravity [24]. However, the actual sliding distance (L) is reduced due to energy losses, such that the ratio of L/L_0 is less than 1. For example, Antonini et al. (2014) measured the sliding distance of water drops rebounding on a SHP surface, and found that $L/L_0 = 0.3$, indicating that the drop travelled only about a third of the idealized sliding length [25]. Although drop sliding length has been measured before, previous reports have either studied the sliding of drops on a liquid surface [24], or else

have measured sliding on a SHP surface but not described the underlying physics [25]. Thus, a theoretical understanding of drop sliding on SHP surfaces is still lacking in the field.

Overall, oblique drop impact studies on SHP surfaces are still very rare, and typically suffer from a major limitation: the terminal falling velocity of a water drop. For millimetric droplets, even if generated a meter above the sample surface, the falling velocity will reach only about 2 m/s. Since the normal impact velocity is further reduced by the tilt angle of the surface (θ), this configuration severely confines the experimental space available to the researcher. In practice, this creates a tradeoff in which impacts may be studied either at high We_n or high AOI, but not both. In response, many reports have operated only at low surface tilt angles, below 30° [23, 26]. Others have chosen to hold θ constant throughout their experiments [22, 27], or else to hold v_d as the independent variable, while changing θ [25]. Although these approaches are practical in the lab, they compound the normal and tangential components of the impact velocity, and thus cannot explain how each individual component affects the impact dynamics. Consequently, the current body of literature provides only a preliminary understanding of the oblique drop impact process on SHP surfaces, and cannot comprehensibly predict drop impact behaviour over a wide range of Weber numbers and angles.

To surpass these limitations, we have designed an experimental apparatus that accelerates a tilted sample surface into a generated droplet, allowing us to test any AOI and impact velocity desired. Thus, we have the unique ability to answer a critical question in the field: for drops impacting with the same normal Weber number, how does the behaviour change as the angle of incidence is increased? Hence, we have tested impacts at twenty different impact conditions: five normal Weber numbers ranging from 3 to 80, each at four different angles of incidence, ranging from 0° (normal impact) to 60° (highly oblique). From this perspective, we aim to provide a new,

comprehensive understanding and predictive power for the sliding length and maximum spread diameter of oblique drop impacts on SHP surfaces under any conditions. This paper constitutes part I of a two-part publication, and focusses on the sliding length and maximum spread diameter of oblique impacting drops on SHP surfaces. In part II, our discussion will continue onto the topics of the contact time and restitution coefficient of rebounding drops [28]. Of these four parameters, only the maximum spread diameter has previously been studied while holding We_n as the independent variable [21], and therefore our analysis on the other three parameters is entirely novel.

EXPERIMENTAL

Our SHP sample surface was fabricated via femtosecond laser micromachining. The substrate used was a polished 0.8 mm thick PTFE sheet, with one bondable side (McMaster Carr). The focused laser beam was raster scanned across a 0.8×3 cm patch in order to ablate the material. For full details, refer to our previous report [29]. As depicted in **Figure 2(c)**, the resulting geometry exhibits hierarchical geometry. The nanostructure consists of a 3-dimensional, interconnected, porous network of wiry strands, and is analogous to the laser ablated PTFE surfaces described by Assaf and Kietzig (2017) [30]. To characterize the geometry of the microstructure, we used an Olympus LEXT 4100 confocal microscope, and measured an average peak-to-peak distance of 10.53 μm, a peak-to-valley height of 2.91 ± 1.42 μm, and a maximum roughness value of $R_{max} = 6.50 \pm 0.78$ μm. For further details, refer to **Supporting Note 1**. This surface was bonded onto an aluminum sample holder using epoxy (H.L. Plasto, 1402).

To characterize the wetting properties of the sample surface, a Data Physics OCA 15E goniometer was used to measure the dynamic contact angles of water droplets. Beforehand, the

sample was cleaned ultrasonically in an acetone bath. Once dry, a 4 µL drop was placed gently on the superhydrophobic surface. The volume was increased to 7 µL at a rate of 0.1 µL/s. Then, after a 5 second pause, the volume was reduced to 1 µL at the same rate. Averaging over three sessile drop tests, we found that the surface's advancing contact angle is 157.6 ± 2°, the receding contact angle is 156.2 ± 2°, and the contact angle hysteresis is 1.4 ± 0.7° (±2 st. dev.).

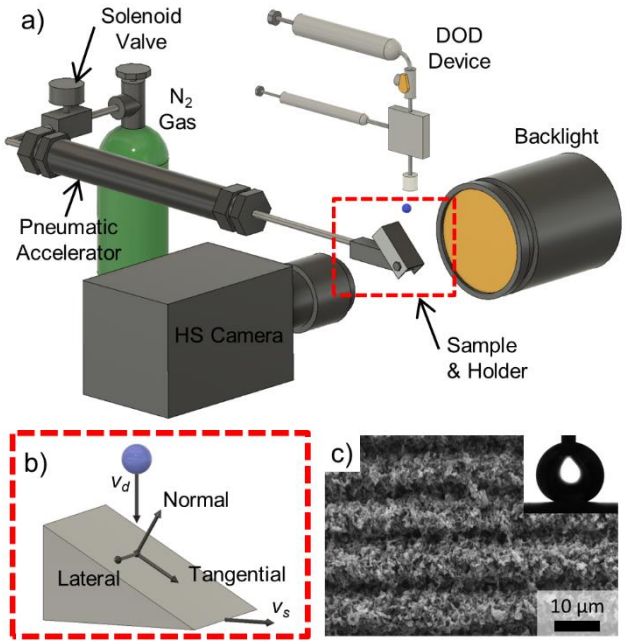

Figure 2. (a) 3D schematic of the drop impact apparatus. (b) Visualization of the orientation of the experiment. The camera is aligned so that the normal and tangential dimensions are visible, but the lateral direction is not observed. (c) Scanning electron microscope image of the sample SHP surface. The inset shows a droplet advancing on the surface during goniometry.

Figure 2(a) provides a schematic of the experimental setup. The sample holder, which can be tilted to any angle from 0 - 90°, is mounted on an aluminum rod, which is driven by a pneumatic accelerator. The sample is oriented such that the drop's sliding direction is over to the crests and

troughs of the microstructure (pictured in **Figure 2(c)**), not along them. The high-speed camera (Photron SA5), equipped with a Navitar Macro Zoom 7000 lens, is placed facing perpendicular to the path of the sample surface in order to capture a side view of the drop impact. An AI SL185-WHI-IC Ultra Bright Spot Light (Optikon Corp.) provided backlighting. Water droplets were produced by a drop-on demand (DOD) generator. For full details on this device, refer to Wood el al. (2018) [31]. The drops generated had an average diameter of 1.29 ± 0.06 mm (± 2 st. dev.). An Arduino Mega 2560 microcontroller prototyping board (Arduino Company) was used to activate the DOD device and the pneumatic sample accelerator in synchronization with the high-speed camera.

Measurement of the drop sliding distance (L) and spread diameter (D) were performed using MATLAB codes, which analyzed high-speed video snapshots. For the sliding distance, the center of mass of the droplet was determined at both the moment of impact and the moment of drop detachment from the surface, and the tangential displacement was measured. The spread diameter was measured for each frame at the surface-air interface.

Throughout this report, time is presented in dimensionless form with respect to the inertial-capillary timescale ($\tau_{ic} = \sqrt{\rho {D_0}^3/8\sigma}$), such that $t^* = t/\tau_{ic}$. This timescale was originally derived by Richard et al. (2002), and is related to the vibrational period of the drop [3, 10]. Lengths are also generally presented in dimensionless form with respect to the original drop diameter, so that $D^* = D/D_0$. All drop impacts were performed on the same sample surface, which was rinsed with acetone between experiments. And, after all experiments were completed, the surface was re-analyzed by optical microscopy, which confirmed that no major deformation or damage occurred. Unless otherwise stated, all values presented for the sliding length and spread diameter in this report are the average of 3 measurements. All margins of error and error bars represent two

standard deviations of the data, plus the equivalent length of 1 pixel when measuring L/L_0 and D^*_{max}. The error bars for the measurements of L/L_0 also include an error analysis on the complex shape of the droplet during impact, as described in **Supporting Note 2**. Multi-variable curve fitting (**Equation 9** & **11**) was performed using MATLAB's NonLinearModel function.

Table 1 outlines the average values of We_n and the AOI in our experiments. Note that in the text and figure legends throughout this report, we will refer to the nearest integer value (for example AOI = 60° instead of 60.2°) for brevity. The exact conditions of an impact are stated where relevant.

Table 1. Data set average values of the normal Weber number and angle of incidence among experiments.

We_n
2.9 ± 0.3
8.8 ± 1.3
23.7 ± 3.0
45.7 ± 3.6
79.8 ± 3.8
AOI (°)
0.5 ± 1.7
29.5 ± 4.3
45.5 ± 2.5
60.2 ± 2.0

RESULTS & DISCUSSION

SLIDING LENGTH

Over the course of an oblique drop impact, the droplet not only spreads radially, but also travels across the surface tangentially. We define the drop sliding length, L, as the distance travelled by the drop's center of gravity while in contact with the surface. This parameter is illustrated by a set of video snapshots in **Figure 3(a)** (original video available in Supporting Information). In each image, the initial impact center is marked by a blue □, the center of mass of the drop's current position is projected onto the surface as a red ○, and the position predicted by ideal sliding (**Equation 2**) is marked by the green △. Note that with respect to the surface, the liquid gradually moves leftwards, away from the impact center. Since the surface moves rightwards in our experimental configuration, this indicates that the droplet is sliding tangentially 'downstream'. Over the course of the impact, the drop continues to slide downstream, and the final frame shows the length of L, which is the final distance between the drop (○) and the impact center (□) at the moment of detachment. Due to adhesion forces, L is shorter than L_0, the idealized sliding length. By measuring the ratio L/L_0, we aim to understand the drag forces acting on the droplet during the impact process.

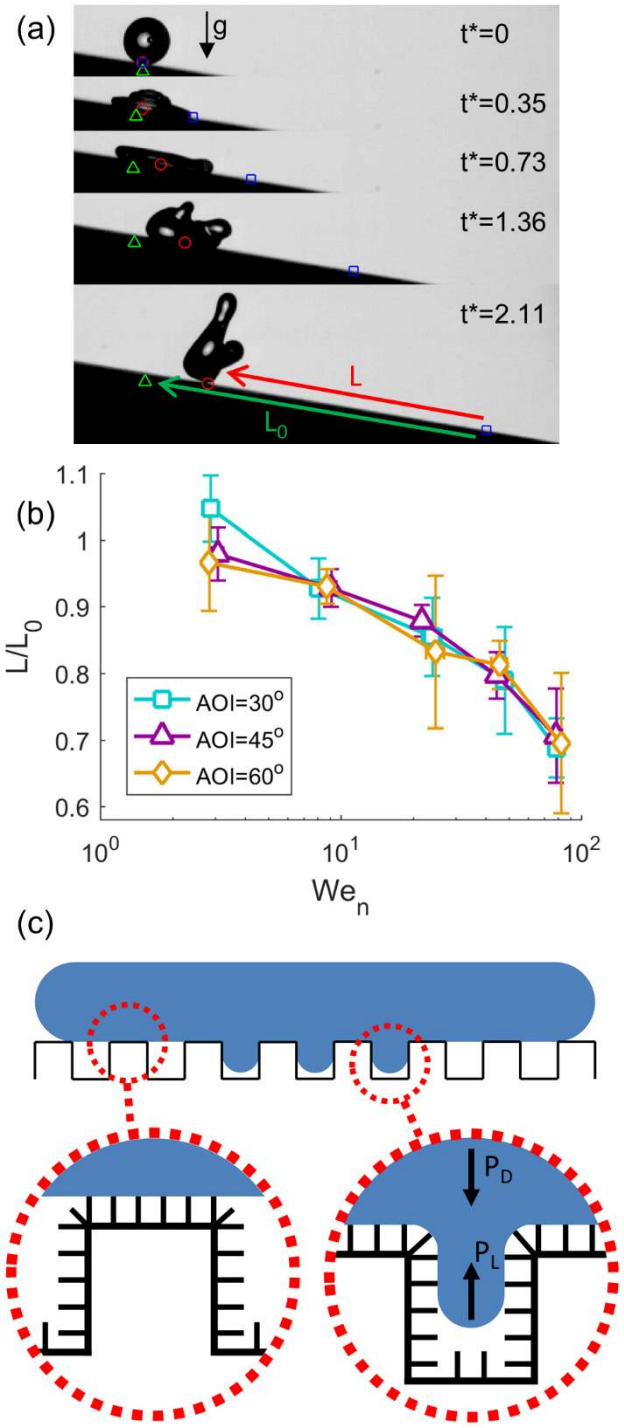

Figure 3. (a) Video snapshots of a drop impact ($We_n = 25.7$, AOI = 62.4°). As the surface moves to the right, so does the impact center (blue □). Also marked are the drop's projected center of mass on the surface (red ○) and the position predicted by **Equation 2** for idealized sliding (green

∆). In the last image, the sliding length (L) and the ideal sliding length (L_0) at the moment of detachment are indicated by arrows. The black arrow indicates the direction of gravity. (b) plot of L/L_0 versus We_n, for three different angles of incidence. (c) Illustration of solid-liquid contact occurring between the drop and SHP surface during impact. The left circle illustrates contact occurring between the spreading lamella and the topographical peaks. The right circle illustrates additional contact occurring between the liquid penetrating the microscopic pores and the solid structure within. The arrows represent the competing Laplace pressure and dynamic impact pressure.

Figure 3(b) plots L/L_0 for each angle and Weber number tested. At the lowest impact speed ($We_n = 3$), the value of L/L_0 is very close to 1, indicating that the drop's motion is essentially unhindered by the surface. As We_n is increased, L/L_0 decreases, reaching values as low as 0.71 for $We_n = 80$. This negative correlation indicates that the tangential movement of the droplet is hindered by its interaction with the surface, and that this effect is more significant at higher We_n. To explain this observation, we consider the interfacial interaction between the drop and the superhydrophobic surface. In the Cassie wetting state, most of the liquid is in contact with trapped air pockets, and only a small fraction of the liquid wets the solid. This solid-liquid contact is illustrated in **Figure 3(c)**, which provides a zoomed view of the interface both beneath the lamella, and in the microscopic pores during impact. As shown in the left circle, the drop's lamella stretches out radially, making contact with the topographical peaks of the surface. And, as illustrated in the right circle, the dynamic impact pressure (P_D) also pushes the liquid into the microstructure of the surface at the center of the impact site [11, 17]. Both of these sources of solid-liquid contact contribute to adhesion, hindering the drop's movement across the surface and resulting in the

observed difference between L and L_0. In addition, impacts occurring at higher We_n apply a greater P_D on the penetrating liquid, which competes with the antiwetting Laplace pressure (P_L) and results in deeper penetration of the liquid into the microstructure of the surface [17]. This competition between opposing pressures can be estimated quantitatively; the gap between each crest of our surface's microstructure is 10.53 μm, which equates to a maximum antiwetting (Laplace) pressure of approximately P_L = 25 kPa. Next, the dynamic impact pressure can be estimated based on the results of Ryu et al. (2017), who analyzed the penetration of water drops through a SHP mesh that is comparable to our surface, and found that $P_D \approx 2.78\rho {v_{n1}}^2$ [19]. Accordingly, in our highest-We_n experiments (We_n = 79.8, v_{n1} = 2.1 m/s), we estimate that P_D = 12 kPa. Therefore, since P_D is lower than P_L in our experimental regime, the meniscus of the liquid front is not expected to fully penetrate the microstructure. However, the increased P_D of higher-speed impacts will still increase the penetration depth, thereby increasing the area of solid-liquid contact. This relationship between the applied pressure on a droplet and the area of contact is supported by previous work from our research group, which characterized the partial penetration into our type of superhydrophobic surface using confocal microscopy through a liquid immersion lens [32]. The increased contact area within the microstructure, coupled with the lamella's increased spread diameter at high We_n, cause the drop to experience greater adhesion on the surface, resulting in decreased values of L/L_0.

Given this understanding, it is interesting that L/L_0 shows a clear variation with We_n, but not with the AOI. Comparing the data for AOI = 30°, 45°, and 60° in **Figure 3(b)**, no clear tend emerges. This lack of correlation is peculiar because, as we will demonstrate in our discussion of the spreading diameter, highly oblique (high AOI) impacts spread over a greater surface area, up to 45% larger than the spread area of normal impacts. Since wider spreading of the lamella should contribute towards more contact sites between the liquid and surface (as illustrated in the left circle

in **Figure 3(c)**), we had expected that higher-AOI impacts would exhibit greater adhesion. Instead, we found that L/L_0 and AOI are not correlated, and therefore that the drop's adhesion is unrelated to its spread area on the surface. This observation could indicate that, of the two sources of solid-liquid contact described above, the contact occurring between the outstretched lamella and the surface contributes only nominally to the overall adhesion between the drop and surface. In that case, the liquid's penetration into the microstructure of the surface (right circle in **Figure 3(c)**) must be the primary source of adhesion. Since partial penetration increases with impact velocity but not with the angle of incidence [17], this would explain why L/L_0 does not vary with the AOI in our experiment.

For comparison, we consider the work of Antonini et al. (2014), who also measured water drops sliding on a SHP surface [25]. For impacts occurring in the range of $We_n = 3$ to 350, they found a consistent value of $L/L_0 = 0.3$, indicating that adhesion caused the droplet to travel only about a third of the ideal sliding length. This observation is in stark contrast to our own results, for which we observed much higher values of L/L_0. The discrepancy likely stems from a difference in adhesion properties between the two surfaces, which can be explained by considering the adhesion at the liquid-solid interface. As the drop impacts the surface and penetrates into the porous structure (**Figure 3(c)**), an interface is formed at each contact point between the liquid and the nanostructure within the pores. The work required to separate such an interface can be quantified by the practical work of adhesion, $W_p = \sigma\ (1 + \cos(RCA))$, where RCA is the receding contact angle of the liquid [33, 34]. And Xiu et al. (2008) have demonstrated that the W_p required to separate a liquid from a superhydrophobic surface is directly proportional to the magnitude of the contact angle hysteresis, i.e. $\sigma\ (1 + cos(RCA)) \sim \cos(ACA) - \cos(RCA)$ [35]. Accordingly, surfaces with lower CAH are known to have lower drop adhesion [35]. Our SHP surface has a CAH of only 1.4°, indicating

remarkably low adhesion between the drop and surface. In contrast, Antonini's surface had a CAH of 15°, indicating much stronger drop adhesion. For a sliding water droplet, this added adhesion increases the drag experienced by the drop, reducing the length it travels across the surface, and thereby the value of L/L_0.

It is also notable that, where we observed a negative correlation between L/L_0 and We_n, Antonini found that L/L_0 remained unchanged as We_n varied [25]. We attribute this discrepancy, as well as the change in adhesion strength between Antonini's surface and our own, to topographical differences between the two surfaces tested. Although both SHP surfaces were composed of PTFE, Antonini's surface was created via acid etching, resulting in a single-scale topography with random roughness [25]. In contrast, our SHP surface has a hierarchical topography, consisting of a wavy microstructure, in turn composed of a wiry nanostructure (shown in **Figure 2(c)**). Generally speaking, hierarchical SHP surfaces exhibit less solid-liquid contact than single-scale topographies, leading to lower adhesion [12]. This explains why L/L_0 was higher on our surface.

SPREADING DIAMETER

Next, we consider the diameter of contact (D) between the spreading lamella and the superhydrophobic surface. **Figure 4(a)** provides video snapshots of an oblique impact spreading on our SHP surface (original video available in Supporting Information). In these images, the blue square marks the initial impact center, and the red circles mark the contact points of the lamella's front (left) and tail (right), such that D is equal to the distance between them (as illustrated for the snapshot at $t^* = 0.22$). Note that due to the rightwards movement of the surface, the contact point on the left is actually the lamella's downstream side (the front), and the contact point on the right is the upstream tail of the drop as it slides. For $t^* = 0.01$ - 0.22, we observe the initial spreading

of the lamella outwards from the impact center. Thereafter, as surface tension causes the lamella to retract ($t^* \geq 0.73$), the contact diameter gradually decreases, and the droplet detaches from the surface immediately after $t^* = 2.08$.

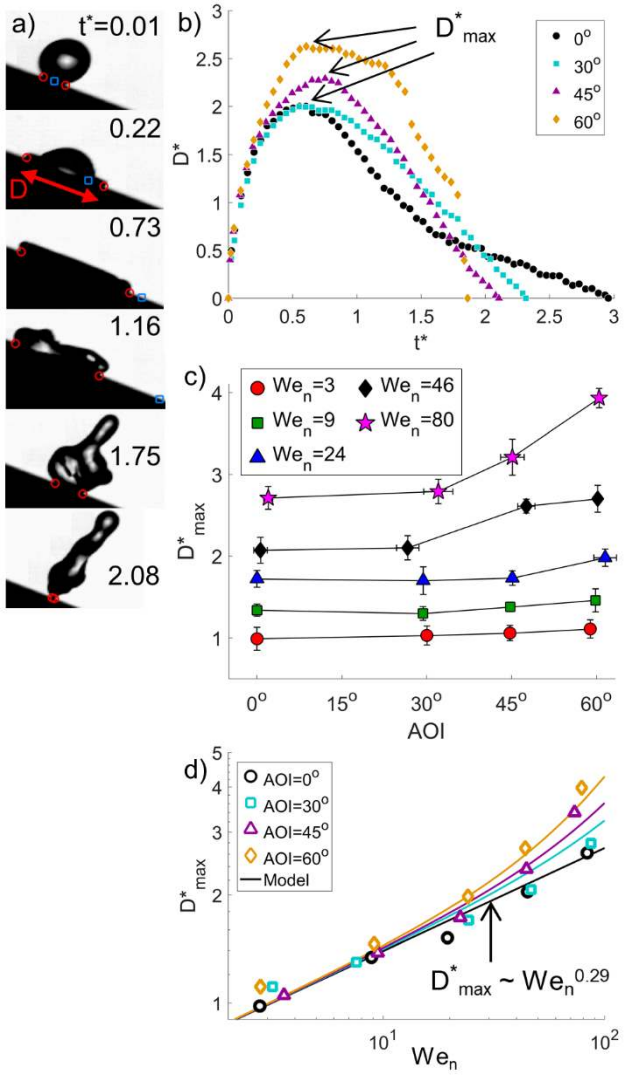

Figure 4. (a) Video snapshots illustrating the contact diameter of an oblique impact ($We_n = 45.1$, AOI = 43.4°). The blue square marks the initial impact center. The red circles mark the contact points of the lamella's front (left) and tail (right). (b) The dimensionless contact diameter of the lamella over time for four representative impacts at $We_n = 46$. Exact parameters are $We_n = 45.1$

& AOI = 0.4°, $We_n = 47.1$ & AOI = 26.3°, $We_n = 45.1$ & AOI = 43.4°, $We_n = 47.6$ & AOI = 60.2°. (c) The average dimensionless maximum spread diameter for impacts at each We_n and AOI tested. (d) The average dimensionless maximum spread diameter plotted on logarithmic axes. The lines represent our model (**Equation 9**).

Figure 4(b) plots the dimensionless spread diameter (D^*) over the course of four impacts, each occurring at $We_n = 46$, but with different AOI (0°, 30°, 45°, 60°). For each impact, D^* reaches its maximum extension (D^*_{max}) within the range of $t^* = 0.6$ to 0.8. Thereafter, the diameter recedes back towards the liquid bulk until the contact points meet at a single position, from which the drop detaches from the surface. For the interested reader, **Supporting Note 3** presents the same data as **Figure 4(b)**, but tracks the positions of the lamella's contact points (red circles in **Figure 4(a)**), instead of the diameter between them.

Where **Figure 4(b)** provides a dynamic view of the drop spreading for the specific case of $We_n = 46$, the average value of D^*_{max} for all impact conditions tested is plotted in **Figure 4(c)**. This data is also presented logarithmically in **Figure 4(d)**. For normal drop impacts (AOI = 0°), we observe that as We_n increases (i.e. higher velocity impacts), D^*_{max} increases monotonically. Over the range tested, D^*_{max} changes from as low as $D^*_{max} = 1$ at $We_n = 3$ (such that the contact diameter spreads only as wide as the original drop diameter for this low-We_n scenario), to as high as $D^*_{max} = 2.6$ for $We_n = 80$. Applying a linear regression fit to this data, we find that the relationship between D^*_{max} and We_n scales as:

$$D^*_{max} = 0.72\, We_n^{0.29} \qquad \textbf{Equation 3}$$

Represented by the black line in **Figure 4(d)**, this relationship provides a good fit for the data ($R^2 = 0.99$), and is consistent with previous reports which found a relationship in the range of $D_{max} \sim We_n{}^{1/4}$ to $D_{max} \sim We_n{}^{0.31}$ [4, 5, 9, 13, 21, 22].

While the above correlation is well-established for normal impacts, our experiments at oblique impact angles reflect a more complex relationship between D^*_{max} and We_n. At each We_n tested, the magnitude of D^*_{max} increases as AOI is raised. Also, this trend is far more pronounced for impacts at greater We_n. For example, in the case of $We_n = 46$, as AOI is increased from 0° to 60°, we observe a significant increase from $D^*_{max} = 2.1$ to 2.7. In contrast, over the same range of angles for $We_n = 3$, we observe only a marginal increase from $D^*_{max} = 0.99$ to 1.11. We attribute both of these trends to the drag experienced by the droplet as it slides across the SHP surface. As the drop's inertia carries it downstream and away from the impact center, adhesion causes the liquid in contact with the surface to resist movement. This creates a stretching effect, as the lamella's front continues to extend downstream while the tail lags behind. And, since drops impacting at higher AOI have greater tangential velocity, they travel further across the surface, experiencing more of this stretching effect. This explains why D^*_{max} increases with AOI. Furthermore, higher-We_n impacts penetrate deeper into the surface's microstructure, causing greater adhesion between the drop and surface. Consequently, drops impacting at higher We_n experience more drag during sliding, and therefore stretch to a greater diameter. This explains why the difference in D^*_{max} between normal and oblique impacts is more significant at high We_n.

Based on these results, we have derived a model to predict D^*_{max} for any We_n and AOI. To begin, we consider two components that contribute to the spreading diameter, which are illustrated in **Figure 5(a)**. The first is the spreading diameter that would be reached by a drop impacting at normal AOI. We will call this length D^*_{normal}, and have already shown that $D^*_{normal} =$

$0.72\ We_n^{0.29}$ on our surface (**Equation 3**). The second component of our model, which we call the stretching length *(S*)*, accounts for the stretching effect caused by drag while the drop slides across the surface. Note that S^* is not calculated with respect to any location on the surface, but instead accounts for the overall widening of the drop's footprint on the surface due to the stretching effect of drag forces. Hence, (S^*) is equal to the increase in the maximum spreading diameter reached by an oblique impact, versus D^*_{normal} of a normal impact. Therefore, by definition, the dimensionless maximum spread diameter of an impacting drop is given by the summation:

$$D^*_{max} = D^*_{normal} + S^* \qquad \textbf{Equation 4}$$

Next, we seek to calculate the dimensionless stretching length (S^*) in terms of known variables. The stretching length of the drop increases for droplets with a greater sliding length on the surface, and also for drops which experience more adhesion on the surface, which is related to partial penetration, and therefore to We_n. Accordingly, we expect that S^* is positively correlated with both the dimensionless ideal sliding length (L_0^*), and with We_n. To determine the exact relationship, **Figure 5(b)** plots S^* versus $L_0^* \cdot We_n$. As indicated by the black line in the figure, we can assume a positive, linear correlation ($R^* = 0.90$):

$$S^* \sim L_0^* \cdot We_n \qquad \textbf{Equation 5}$$

To make this equation useable, we need to state L_0^* as a function of We_n and the AOI. So, recalling **Equation 2**, and ignoring the effect of gravity (whose role is minor), the drop's ideal sliding length is approximately equal to $L_0 = v_{t1} t_c$. And, as demonstrated by Richard et al. (2002), the contact time of a rebounding drop (t_c) is governed by the scaling relationship $t_c \sim \sqrt{\rho {D_0}^3/\sigma}$ [3]. Therefore, the dimensionless ideal sliding length of an impacting drop is proportional to:

$$L_0^* = \frac{L_0}{D_0} \sim v_{t1}\sqrt{\rho D_0/\sigma} \qquad \textbf{Equation 6}$$

Then, substituting $v_{t1} = v_{n1} \cdot \tan(AOI)$ (rearranged from **Equation 1**), we find that L_0^* can be related to We_n and the AOI by the following correlation:

$$L_0^* \sim tan(AOI) \cdot \sqrt{We_n} \qquad \textbf{Equation 7}$$

Substituting **Equation 7** back into **Equation 5**, the stretching length can be stated in terms of known variables:

$$S^* \sim tan(AOI) \cdot We_n^{3/2} \qquad \textbf{Equation 8}$$

Finally, substituting **Equation 8** along with **Equation 3** (for D^*_{normal}) back into **Equation 4**, we arrive at our model for the maximum spread diameter of an oblique impact:

$$D^*_{max} = 0.72\, We_n^{0.29} + 9.9 \times 10^{-4}\, tan(AOI) \cdot We_n^{3/2} \qquad \textbf{Equation 9}$$

where the factor of 9.9×10^{-4} was determined by the method of least squares regression, and has a 95% confidence interval of $\pm\, 1.3 \times 10^{-4}$. In **Figure 5(c)**, the solid lines denote **Equation 9** along with the original data. Our model provides a good fit, matching the data well for each We_n and AOI tested.

For comparison, we have also plotted another model derived by Yeong et al. (2014), who presented the following equation [21]:

$$D^*_{max} = 0.9\, We_n^{1/4} + c_3 We_t \qquad \textbf{Equation 10}$$

where c_3 is a scaling factor, and We_t is a tangential Weber number, $We_t = tan^2(AOI) \cdot We_n$. Much like our own model, the first term of **Equation 10** describes D^*_{normal}, while the second term is analogous to S^*. But, as explained in the introduction, D^*_{normal} varies depending on the surface tested. Therefore, in order to adapt **Equation 10** to our own surface, we will replace the original first term of $0.9\, We_n^{1/4}$ with our own measurement of $0.72\, We_n^{0.29}$. Then, using the method of least squares regression, we find an optimized value of $c_3 = 0.0051$ for our surface. Including

these changes, and substituting the formula for We_t above, Yeong's model transforms into the following equation, which is adjusted to the properties of our particular surface:

$$D^*_{max} = 0.72\, We_n{}^{0.29} + 0.0051\, tan^2(AOI) \cdot We_n \qquad \textbf{Equation 11}$$

Equation 11 is denoted by the dashed lines in **Figure 5(c)**, and also provides a good fit for the data from AOI = 0° to 60°.

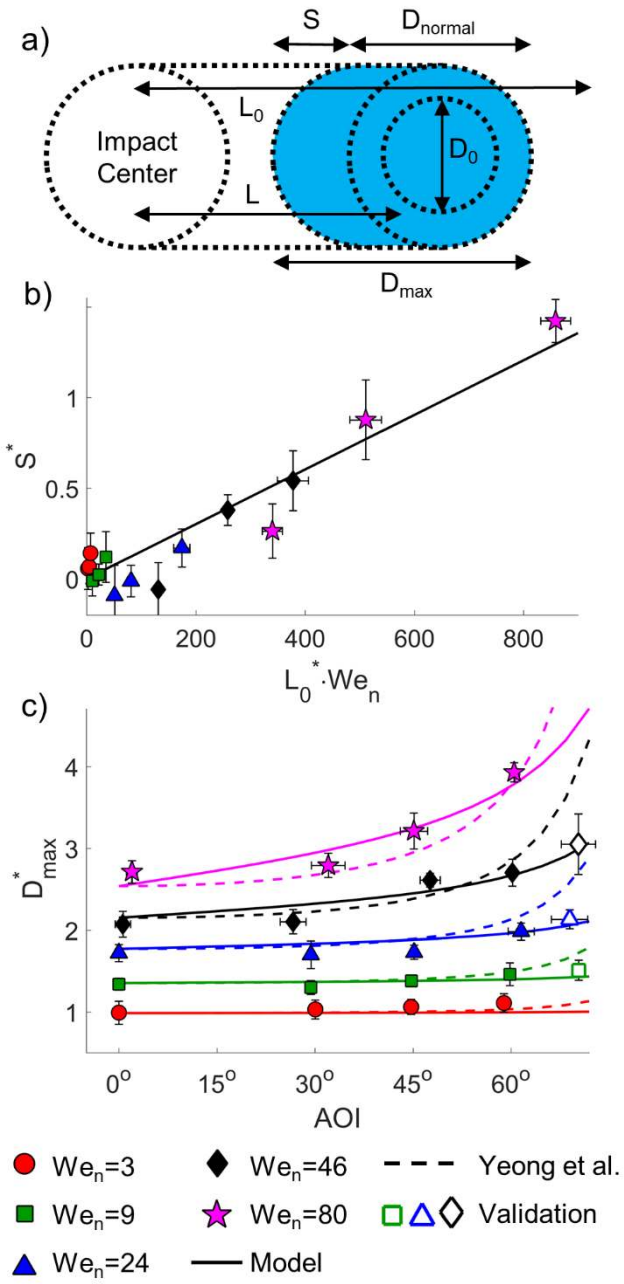

Figure 5. (a) Schematic of the spread diameter of an oblique impacting drop. The maximum spread diameter can be viewed as two components, the normal spread diameter, and the stretching length. (b) The stretching length of oblique drop impacts versus the product of the ideal sliding length and normal Weber number. The black line indicates a linear correlation (**Equation 5**). (c) Maximum spread diameter data from experiments. The solid line represents our model (**Equation 9**), and the dashed line is the model by Yeong et al. (**Equation 11**) [21]. The open faced markers indicate

validation experiments performed to confirm our model's predictive power ($We_n = 8.8$ & AOI = 70.4, $We_n = 22.5$ & AOI = 69.0, $We_n = 44.7$ & AOI = 70.4).

For both models tested, fitting was performed using data from impacts in the range of 0 - 60°. Then, to confirm the predictive power of our model, we performed additional impacts at AOI = 70° and $We_n = 9$, 24, and 46, as indicated by the open markers in **Figure 5(c)**. From these validation experiments, the measured values of D^*_{max} are all very close to our model's predictions, with an average margin of error of only 4%. This proves that **Equation 9** is successful in predicting the maximum spread diameter even at higher angles of incidence. In contrast, **Equation 11** seems to overpredict each value of D^*_{max} with an average margin of error of 21%. Therefore, where both models performed equally well in the range of AOI = 0 to 60°, our validation experiments demonstrate that our model is more accurate in the case of highly oblique impacts (AOI > 60°). In addition, our model has the advantage of a stronger theoretical backing. Although Yeong's model is very similar, the second term of **Equation 11** has little physical meaning [21]. As a result, at high AOI this term grows very quickly, which is why **Equation 11** overshot the values of D^*_{max} at AOI = 70°.

Using our model for the maximum spread diameter, we are also interested in predicting the total spread area of the drop. To do this, we must consider the lateral spreading of the lamella (see **Figure 2(b)** for clarification). In the side-view images presented so far, the lateral spread is not measurable, since it occurs through the plane of the images. Thus, as shown in **Figure 6**, we performed experiments with the camera positioned above the surface, looking down to observe the full spread area. We measured two drop impacts at an average of $We_n = 44.5 \pm 2.5$ and AOI = 44.1 ± 0.1° (**Figure 6(a)).** In the tangential direction, we measured a maximum spread diameter of

$D^*_{max} = 2.64 \pm 0.21$, which matches well with our average measurement of 2.61 from **Figure 4(c)**. In the lateral direction, we measured $D^*_{max} = 2.16 \pm 0.08$, which is close to our measurement of $D^*_{normal} = 2.07$ for impacts at normal angle of incidence (AOI = 0°). We found the same behaviour from our measurements at $We_n = 23.9 \pm 2.5$ and AOI = 60.2 ± 0.0° (**Figure 6(b)**); in the tangential direction, we measured an average of $D^*_{max} = 2.04 \pm 0.05$, which matches the value of 1.98 from **Figure 4(c)**; and in the lateral direction, we found an average of $D^*_{max} = 1.68 \pm 0.06$, which matches the value of $D^*_{normal} = 1.72$ at $We_n = 24$. Therefore, all of our measurements demonstrate that for oblique drop impacts, the lateral spread is similar to D^*_{normal} of a drop impacting at AOI = 0°, and is not greatly affected by the angle of incidence. Indeed, **Figure 6** clearly demonstrates that oblique impacting droplets spread into an ellipsoid, with the minor radius matching that of an equivalent normal impact, and the major radius being stretched by the oblique nature of the impact. Therefore, oblique drop impacts spread over a greater total surface area than normal impacts do, and must conserve volume by decreasing in thickness. Accordingly, we suggest that the maximum spread area of an oblique drop impact is given by the product of **Equation 3** and **Equation 9**:

$$A^*_{max} = \frac{A_{max}}{{D_0}^2} = 0.72\, {We_n}^{0.29}\,(0.72\, {We_n}^{0.29} + 9.9 \times 10^{-4}\, tan(AOI) \cdot {We_n}^{3/2}) \quad \textbf{Equation 12}$$

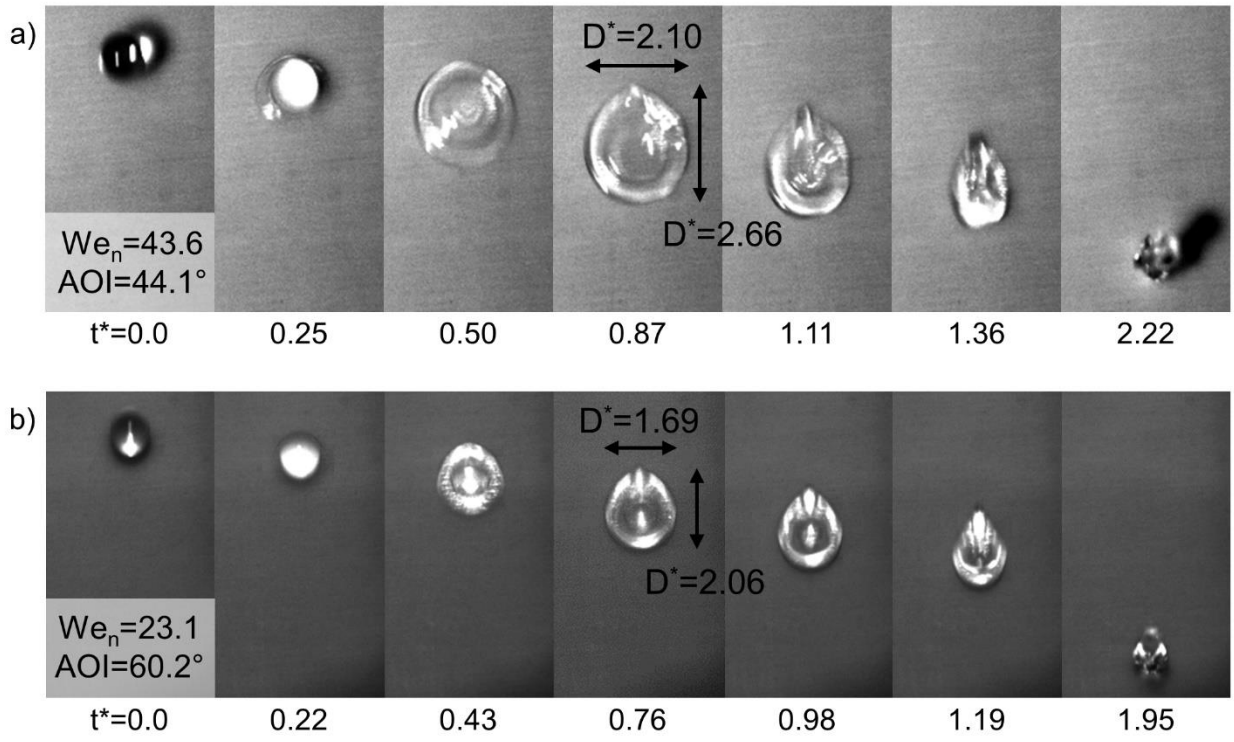

Figure 6. The spreading of a water droplet impacting on our SHP surface, as seen from above. (a) Oblique impact at $We_n = 43.6$ & AOI = 44.1°. (b) Oblique impact at $We_n = 23.1$ & AOI = 60.2°.

The fact that oblique drop impacts spread over an enlarged maximum area than normal impacts leads to another interesting revelation: oblique impacts store more surface energy during maximum deformation (SE_{max}) than normal impacts. We suggest that this is possible due to the drop's kinetic energy in the tangential dimension (KE_t), coupled with the drag experienced by the liquid while sliding across the SHP surface. Drag forces not only cause the drop's perimeter to stretch to a greater D^*_{max}, but also arrest the tangential movement of the drop. In this way, drag allows some fraction of KE_t to be transferred into surface energy during the oblique drop impact process. This energy transfer can be demonstrated quantitatively by considering our sliding length and spreading diameter measurements at $We_n = 80$ and $AOI = 60°$. At these settings, **Figure 3(b)** shows that

L/L_0 is equal to 0.73. Assuming a constant sliding velocity, this indicates a roughly 27% decrease in the drop's tangential velocity (v_t), and hence a 46% decrease in KE_t, since $KE_t \sim {v_t}^2$. Meanwhile, **Figure 5(b)** indicates that D^*_{max} is equal to 3.93, a 45% increase over the normal value of $D^*_{normal} = 2.71$. Considering **Equation 12** for A^*_{max}, this also indicates 45% increase in the surface area of the deformed drop, and thus in SE_{max}. Based on these estimates, it is clear that a portion of the drop's tangential kinetic energy is transformed into surface energy during the impact event.

The drop impact shown in **Figure 6(a)** is almost identical to an experiment by Zhang et al. (2017), who performed above-view imaging of a drop impact at We_n = 40 and AOI = 45° on a superhydrophobic Silicon surface [22]. However, there is a major difference in substrate topography between the two experiments: Zhang's substrate had a random, single-scale topography, whereas our surface has a hierarchical, heterogeneous trench structure. Comparing visually **Figure 6(a)** to Zhang's images, both impacts appear to be essentially identical, stretching into a similar ellipsoidal shape at their maximum extension. In fact, Zhang's measurements of D^*_{max} = 2.3 in the tangential direction and 2.1 in the lateral dimension match **Equation 12** to within 2% accuracy. Based on these comparisons, we believe that our analysis on drop spreading is generalizable to SHP surfaces with different geometric structures.

However, concerning the application of our models for D^*_{max} and A^*_{max}, it is important to note that both equations pertain to the case of non-pinning, non-splashing impacts. Furthermore, when applying **Equation 9 & 12** to other SHP surfaces, the equations may need to be adjusted to the surface in question. For example, the term $0.72\,{We_n}^{0.29}$ (representing D^*_{normal}) arises in both **Equation 9 & 12**, but does not represent the general case for all SHP surfaces. As per the introduction, drop impact studies on other SHP surfaces have reported varying scaling factors for

this relationship, ranging from $D_{max} \sim We_n^{1/4}$ to $D_{max} \sim We_n^{1/2}$ [4-6, 9, 13, 21-23]. Moreover, our analysis of the sliding length of drops proved that SHP surfaces of varying geometry can have entirely different adhesion properties. Thus, given that the second term of **Equation 9** accounts for the effect of adhesion on the spread diameter, the factor of 9.9×10^{-4} can also be expected to vary depending on the surface. Nevertheless, although elements of the equations may vary, our method of derivation can be applied to any SHP surface, and can accurately predict the spreading behaviour of drops at any We_n and AOI.

CONCLUSIONS

The sliding length of oblique impacting droplets was measured. We found that the drops' movement across the surface was hindered by adhesion forces. Impacts occurring at low We_n were essentially unhindered, with L/L_0 close to 1, while higher-We_n impacts experienced more drag during sliding, such that L/L_0 was reduced. We relate this trend to the increased partial penetration of liquid into the structure of the superhydrophobic surface that occurs in higher-We_n impacts, which results in an increase in the solid-liquid contact in the pores of the surface, and hence greater adhesion. Further, by comparing our sliding length measurements to previously reported values, we discovered that geometrical differences greatly affect the adhesion strength of surfaces. As a result, hierarchical surfaces can allow drops to slide up to three times further than surfaces with single-scale geometry.

The spreading diameter of impacting drops was also measured at varying We_n and AOI. For impacts occurring at normal angle of incidence, we found that the maximum spread diameter (D^*_{max}) is correlated with We_n by the relationship $D^*_{max} = 0.72\, We_n^{0.29}$, which is consistent with previous measurements. For oblique impacts, we discovered that due to adhesion, the drop's

tangential motion across the surface causes a stretching effect, increasing D^*_{max} for impacts at higher AOI. Furthermore, this stretching effect is more pronounced for impacts occurring at higher We_n. We associate this correlation with the partial penetration of liquid into the pores of the SHP surface, which results in greater adhesion for high-We_n impacts.

Based on these assertions, we derived a model to predict D^*_{max} for any impact, given the We_n and AOI. The model successfully describes D^*_{max} for our entire experimental range. Furthermore, by performing a validation experiment outside of our experimental range, we confirmed the accurate predictive power of our model.

Finally, by positioning the camera above the SHP surface, we measured the spread diameter in both the tangential and lateral directions simultaneously. We found that oblique impacts spread further in the tangential direction than the lateral, such that the drop's overall spread area is elliptical. Based on this observation, and using our equation for D^*_{max}, we derived a formula for the maximum spread area of oblique impacts on SHP surfaces.

ASSOCIATED CONTENT

Supporting Information. Confocal Microscopy Analysis (Supporting Note 1). Error analysis for sliding length measurements (Supporting Note 2). Plot of dimensionless contact positions versus time (Supporting Note 3).

Videos: The original videos of the drop impacts shown in Figures 3 and 4, including markers added by a MATLAB code that calculated the sliding length and spreading diameter.

AUTHOR INFORMATION

Corresponding Author

*Anne-Marie Kietzig, McGill University, Department of Chemical Engineering 3610 University Street, Montreal, Quebec, H3A 0C5, Canada, email: anne.kietzig@mcgill.ca.

Author Contributions

Damon Aboud designed and performed the experiments, and wrote the manuscript. Prof. Anne-Marie Kietzig guided the project and edited the manuscript. All authors have given approval to the final version of the manuscript.

Funding Sources

This work was supported by the Natural Sciences and Engineering Research Council (NSERC) of Canada.

ACKNOWLEDGMENT

The authors acknowledge Dr. Daniel Gagnon of the Institut de Recherche d'Hydro-Québec (IREQ) for the financial support. DA acknowledges Dr. Felipe Aristizabal (McGill University) for helpful discussions, and also Dr. Carlo Antonini (Swiss Federal Laboratories for Materials Science and Technology) for his correspondence regarding drop sliding.

REFERENCES

1. Varanasi, K. K.; Deng, T.; Smith, J. D.; Hsu, M.; Bhate, N. Frost Formation and Ice Adhesion on Superhydrophobic Surfaces. *Appl. Phys. Lett.* **2010**, 97, 234102.

2. Park, J.; Lim, H.; Kim, W.; Ko, J. S. Design and Fabrication of a Superhydrophobic Glass Surface with Micro-Network of Nanopillars. *J. Colloid Interface Sci.* **2011**, 360, 272-279.

3. Richard, D.; Clanet, C.; Quéré, D. Contact Time of a Bouncing Drop. *Nature* **2002**, 417, 811.

4. Tsai, P.; Hendrix, M. H.; Dijkstra, R. R.; Shui, L.; Lohse, D. Microscopic Structure Influencing Macroscopic Splash at High Weber Number. *Soft Matter* **2011**, 7, 11325-11333.

5. Meng, K.; Jiang, Y.; Jiang, Z.; Lian, J.; Jiang, Q. Impact Dynamics of Water Droplets on Cu Films with Three-Level Hierarchical Structures. *J. Mater. Sci.* **2014**, 49, 3379-3390.

6. Kim, H.; Lee, C.; Kim, M. H.; Kim, J. Drop Impact Characteristics and Structure Effects of Hydrophobic Surfaces with Micro-and/or Nanoscaled Structures. *Langmuir* **2012**, 28, 11250-11257.

7. Rioboo, R.; Tropea, C.; Marengo, M. Outcomes from a Drop Impact on Solid Surfaces. *Atomization Sprays* **2001**, 11, 155-165.

8. Yarin, A. Drop Impact Dynamics: Splashing, Spreading, Receding, Bouncing…. *Annu. Rev. Fluid Mech.* **2006**, 38, 159-192.

9. Clanet, C.; Béguin, C.; Richard, D.; Quéré, D. Maximal Deformation of an Impacting Drop. *J. Fluid Mech.* **2004**, 517, 199-208.

10. Bird, J. C.; Dhiman, R.; Kwon, H.-M.; Varanasi, K. K. Reducing the Contact Time of a Bouncing Drop. *Nature* **2013**, 503, 385-388.

11. Maitra, T.; Tiwari, M. K.; Antonini, C.; Schoch, P.; Jung, S.; Eberle, P.; Poulikakos, D. On the Nanoengineering of Superhydrophobic and Impalement Resistant Surface Textures Below the Freezing Temperature. *Nano Lett.* **2013**, 14, 172-182.

12. Koch, K.; Bhushan, B.; Jung, Y. C.; Barthlott, W. Fabrication of Artificial Lotus Leaves and Significance of Hierarchical Structure for Superhydrophobicity and Low Adhesion. *Soft Matter* **2009**, 5, 1386-1393.

13. Deng, X.; Schellenberger, F.; Papadopoulos, P.; Vollmer, D.; Butt, H.-J. r. Liquid Drops Impacting Superamphiphobic Coatings. *Langmuir* **2013**, 29, 7847-7856.

14. Mishchenko, L.; Hatton, B.; Bahadur, V.; Taylor, J. A.; Krupenkin, T.; Aizenberg, J. Design of Ice-Free Nanostructured Surfaces Based on Repulsion of Impacting Water Droplets. *Acs Nano* **2010**, 4, 7699-7707.

15. Li, X.-M.; Reinhoudt, D.; Crego-Calama, M. What Do We Need for a Superhydrophobic Surface? A Review on the Recent Progress in the Preparation of Superhydrophobic Surfaces. *Chem. Soc. Rev.* **2007**, 36, 1350-1368.

16. Barthlott, W.; Neinhuis, C. Purity of the Sacred Lotus, or Escape from Contamination in Biological Surfaces. *Planta* **1997**, 202, 1-8.

17. LeClear, S.; LeClear, J.; Park, K.-C.; Choi, W. Drop Impact on Inclined Superhydrophobic Surfaces. *J. Colloid Interface Sci.* **2016**, 461, 114-121.

18. Lee, C.; Nam, Y.; Lastakowski, H.; Hur, J. I.; Shin, S.; Biance, A.-L.; Pirat, C.; Ybert, C. Two Types of Cassie-to-Wenzel Wetting Transitions on Superhydrophobic Surfaces During Drop Impact. *Soft Matter* **2015**, 11, 4592-4599.

19. Ryu, S.; Sen, P.; Nam, Y.; Lee, C. Water Penetration through a Superhydrophobic Mesh During a Drop Impact. *Phys. Rev. Lett.* **2017**, 118, 014501.

20. Kwon, H.-M.; Paxson, A. T.; Varanasi, K. K.; Patankar, N. A. Rapid Deceleration-Driven Wetting Transition During Pendant Drop Deposition on Superhydrophobic Surfaces. *Phys. Rev. Lett.* **2011**, 106, 036102.

21. Yeong, Y. H.; Burton, J.; Loth, E.; Bayer, I. S. Drop Impact and Rebound Dynamics on an Inclined Superhydrophobic Surface. *Langmuir* **2014**, 30, 12027-12038.

22. Zhang, R.; Hao, P.; He, F. Drop Impact on Oblique Superhydrophobic Surfaces with Two-Tier Roughness. *Langmuir* **2017**.

23. Wang, B.-B.; Zhao, Y.-P.; Yu, T. Fabrication of Novel Superhydrophobic Surfaces and Droplet Bouncing Behavior—Part 2: Water Droplet Impact Experiment on Superhydrophobic Surfaces Constructed Using Zno Nanoparticles. *J. Adhes. Sci. Technol.* **2011**, 25, 93-108.

24. Gilet, T.; Bush, J. W. Droplets Bouncing on a Wet, Inclined Surface. *Phys. Fluids* **2012**, 24, 122103.

25. Antonini, C.; Villa, F.; Marengo, M. Oblique Impacts of Water Drops onto Hydrophobic and Superhydrophobic Surfaces: Outcomes, Timing, and Rebound Maps. *Exp. Fluids* **2014**, 55, 1-9.

26. Zhu, J.; Deng, D. Ammonia-Assisted Wet-Chemical Synthesis of Zno Microrod Arrays on Substrates for Microdroplet Transfer. *Langmuir* **2017**.

27. Ramachandran, R.; Sobolev, K.; Nosonovsky, M. Dynamics of Droplet Impact on Hydrophobic/Icephobic Concrete with Potential for Superhydrophobicity. *Langmuir* **2015**.

28. Aboud, D.; Kietzig, A.-M. On the Oblique Impact Dynamics of Drops on Superhydrophobic Surfaces. Part Ii: Restitution Coefficient and Contact Time. *Langmuir* **2018**.

29. Aboud, D. G.; Kietzig, A.-M. Splashing Threshold of Oblique Droplet Impacts on Surfaces of Various Wettability. *Langmuir* **2015**, 31, 10100-10111.

30. Assaf, Y.; Kietzig, A.-M. Optical and Chemical Effects Governing Femtosecond Laser-Induced Structure Formation on Polymer Surfaces. *Mater. Today Commun.* **2018**.

31. Wood, M. J.; Aristizabal, F.; Coady, M.; Nielson, K.; Ragogna, P. J.; Kietzig, A.-M. The Precise and Accurate Production of Millimetric Water Droplets Using a Superhydrophobic Generating Apparatus. *Phys. Fluids* **2018**, 30, 027104.

32. Ahmmed, K. T.; Patience, C.; Kietzig, A.-M. Internal and External Flow over Laser-Textured Superhydrophobic Polytetrafluoroethylene (Ptfe). *ACS Appl. Mater. Interfaces* **2016**, 8, 27411-27419.

33. Meuler, A. J.; Smith, J. D.; Varanasi, K. K.; Mabry, J. M.; McKinley, G. H.; Cohen, R. E. Relationships between Water Wettability and Ice Adhesion. *ACS Appl. Mater. Interfaces* **2010**, 2, 3100-3110.

34. Gao, L.; McCarthy, T. J. Teflon Is Hydrophilic. Comments on Definitions of Hydrophobic, Shear Versus Tensile Hydrophobicity, and Wettability Characterization. *Langmuir* **2008**, 24, 9183-9188.

35. Xiu, Y.; Zhu, L.; Hess, D. W.; Wong, C. Relationship between Work of Adhesion and Contact Angle Hysteresis on Superhydrophobic Surfaces. *J. Phys. Chem. C* **2008**, 112, 11403-11407.

SYNOPSIS

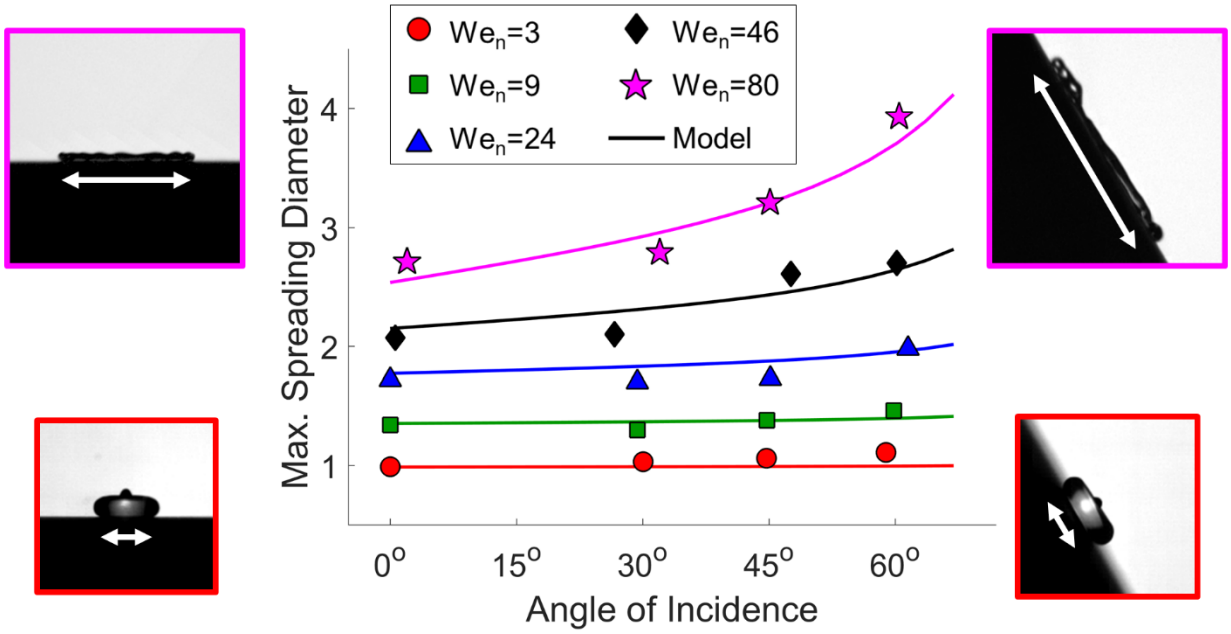

The TOC graphic shows our experimental data for the maximum spreading diameter of drops at different normal Weber numbers and angles of incidence, along with our derived model. The boxes on the sides show snapshots of drop impacts representing the data at the highest and lowest normal Weber numbers tested, and at the highest and lowest angles of incidence tested, in order to illustrate the changes observed across our experimental space.

SUPPORTING NOTE 1: CONFOCAL MICROSCOPY ANALYSIS

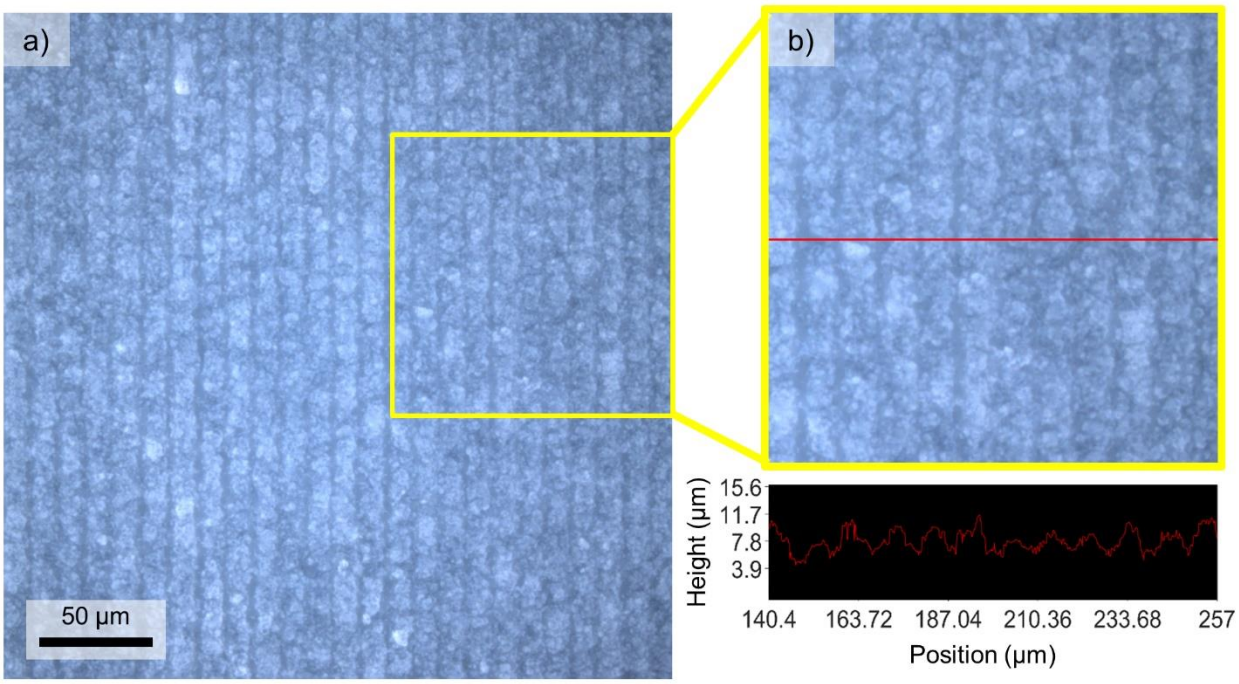

Figure S1. Confocal microscopy analysis of the SHP sample surface after experiments. (a) Micrograph of the surface texture, showing no major deformation or damage. (b) Demonstration of the geometry of the textured surface, using the microscope's software.

In order to characterize the geometry of our sample surface, and also to check for any damage caused by drop impacts, we analyzed the surface using a confocal microscope. **Figure S1(a)** displays a large section of the surface, and demonstrates that there is no appreciable damage to the texture after experiments. **Figure S1(b)** provides a zoomed-in view of a section from (a), along with the height profile of a horizontal line across the middle. By measuring many sections such as this, we determined an average peak-to-valley height of 2.91 ± 1.42 µm, and an average maximum roughness value of R_{max} = 6.50 ± 0.78 µm.

SUPPORTING NOTE 2: ERROR ANALYSIS FOR SLIDING LENGTH MEASUREMENTS

For each data point in **Figure 3(b)** (which plots L/L_0 versus We_n), there are three primary sources of error:

1) Variation in the data: each data point in **Figure 3(b)** represents the average of three sliding length measurements, from different videos. The error associated with the variation in the data (E_{var}) is equal to 2 standard deviations of the data.

2) Pixel error: As shown in **Figure S2(a-b)**, in order to define the profile of the droplet in each frame of the video, our MATLAB program uses a threshold brightness value to identify each pixel in the image as being either part of the droplet, or as background. To account for any misjudgment in this process, we account for the pixel error, $E_{pix}=C/L_0$, where C is the calibration constant of the camera (mm/pixel).

3) Profile error: to track the drop's sliding length (L), the center of mass is estimated based the drop's profile (**Figure S2(b)**). However, since the drop is deformed into a complex shape through its interaction with the surface, the estimated center of mass is subject to some error. In order to quantify this error, each measurement of L is plotted against time, and a linear regression is applied to the data (**Figure S2(c)**). The slope of the regressed line provides the sliding speed of the drop (v_{slide}), such that our measured value of L is equal to the product of the line's slope and the contact time ($L = v_{slide}t_c$). Then, using MATLAB's regress function, we determine the 95% confidence interval of the sliding speed (Δv_{slide}). We assume that this confidence interval reflects the error related to the drop's complex profile, such that the profile error is equal to $E_{pro} = \Delta v_{slide}t_c/L_0$.

Based on the sources of error listed above, the total error presented by the error bars in **Figure 3(b)** is equal to $E_t = E_{var} + E_{pix} + E_{pro}$.

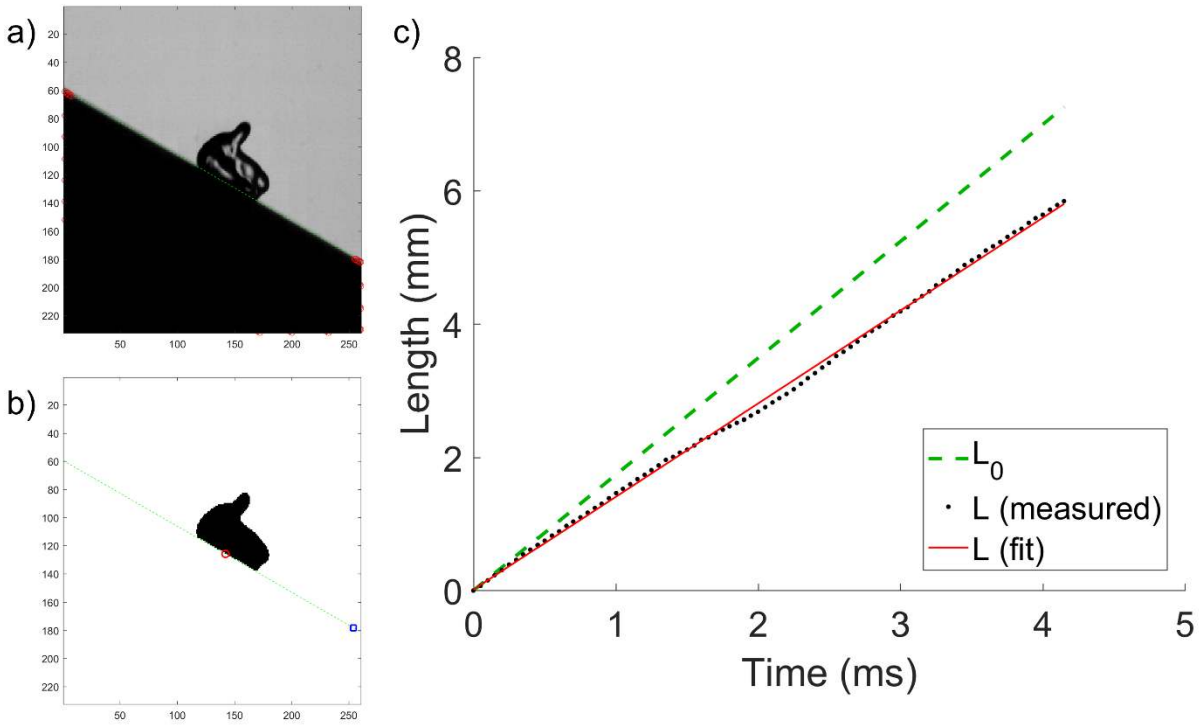

Figure S2. (a) Original snapshot of drop while sliding on the SHP surface. The green line estimates the position of the surface. (b) MATLAB's estimate of the profile of the droplet, and of the center of mass (red circle projected onto the surface). (c) Plot of the drop's estimated sliding length (*L* (measured)) over time, with respect to L_0. The red line is a linear regression of the sliding length data.